A parametric analysis of embedded tissue marker properties and their effect on the accuracy of displacement measurements

Scott Dutrisac[1], MacKenzie Brannen[1], T. Blaine Hoshizaki[2], Hanspeter Frei[1], and Oren E. Petel[1,*]

[1]Department of Mechanical and Aerospace Engineering, Carleton University, Ottawa, ON, Canada K1S 5B6
[2]School of Human Kinetics, University of Ottawa, Ottawa, ON, Canada K1S 5S9
[*]Corresponding author: oren.petel@carleton.ca

Abstract

Datasets obtained from cadaveric experimentation are broadly used in validating finite element models of head injury. Due to the complexity of such measurements in soft tissues, experimentalists have relied on tissue-embedded radiographic or sonomicrometry tracking markers to resolve tissue motion caused by impulsive loads. Dynamic coupling of markers with the surrounding tissue has been a previous concern, yet a thorough sensitivity investigation of marker influences on tissue deformation has not been broadly discussed. Technological improvements to measurement precision have bolstered confidence in acquired data, however precision is often conflated with accuracy; the inclusion of markers in the tissue may alter its natural response, resulting in a loss of accuracy associated with an altered displacement field. To gain an understanding of how marker properties may influence the measured response to impact, we prepared a set of nine marker designs using a Taguchi L9 array to investigate marker design choice sensitivity. Each of these designs was cast into a block of tissue simulant and subjected to repeated drop tests. Vertical displacement was measured and compared to the response of the neat material, which contained massless tracking markers. Medium density and medium stiffness markers yielded the least deviation from the neat material response. The results provide some design guidelines indicating the importance of maintaining marker matrix density ratio below 1.75 and marker stiffness below 1.0 MPa. These properties may minimize marker interference in tissue deformation. Overall, embedded marker properties must be considered when measuring the dynamic response of tissue.

1 Introduction

Optical measurements of deformation are becoming more prevalent in experimental mechanics as full-field strain measurements can be acquired with minimal sample contact (Palanca et al., 2016). Digital image correlation is a technique that involves tracking the motion of speckle patterns to determine displacement and deformation fields on a deforming body (Chu et al., 1985; Schreier et al., 2009). These speckle patterns have primarily consisted of black paint on a white background for optimal contrast. However, some studies have used fluorescence (Hu et al., 2018), epoxy markers (Lauret et al., 2009), and cellular features (Meijering et al., 2012) for tracking displacements of biological tissues. Where spatial resolution or experimental limitations dictate the need for a reduced marker or speckle number density, individual particle tracking algorithms can also be used to determine deformation and strain fields (Li et al., 2016). Due to the nature of these optical methods, this area of research is often concerned with surface deformations, as trackable patterns can only be applied to the surface of a body. This has led to the use of markers that are essentially massless. The massless marker is one whose inertia will not influence the deformation process of the specimen subjected to dynamic loading.

In specimens with internal, and consequently visually inaccessible, regions of interest, particle tracking techniques have been applied using radiographic markers embedded within the region (Karrholm et al., 2006). Radiographic imaging has been used to evaluate displacement and deformation within optically opaque materials (Synnergren et al., 1999). Under radiographic imaging, markers require sufficient density to be radiopaque; however, the concern is that marker inertia is no longer negligible when tracking

deformation under dynamic loading events (Hardy et al., 2007; Whyte et al., 2019). A recent study highlighted that the post-impact migration of markers within brain tissue is a valid concern (Whyte et al., 2019). While ensuring proper coupling of the markers to surrounding materials and negligible marker migration is important, the lack of marker migration is not necessarily a measure of ideal dynamic coupling.

Prior designs of embedded markers were selected in an effort to minimize differences in inertia, either through optimizing marker density (Hardy et al., 2007; Alshareef et al., 2018) or minimizing the overall marker mass (Guettler, 2017). Other approaches to marker tracking within brain tissues have included stiff, low density sonomicrometry crystals to improve marker tracking precision (Alshareef et al., 2018, 2020). However, marker tracking precision does not guarantee the fidelity of dynamic marker coupling or the accuracy of a tissue deformation measurement, as the presence of the markers can significantly change the response of the surrounding tissues during dynamic events. It is important to quantify and ideally minimize the error associated with introducing markers into tissue as cadaveric data are used extensively in the validation of computational head injury models (Zhou et al., 2019; Zhao and Ji, 2020).

While marker inertia is certainly an important property to consider, particularly for capturing realistic rigid body motion, it is not the only parameter of importance in a dynamic loading event. Any physical perturbation to a deformable body (e.g., brain tissue) will propagate as a series of perturbations, as per elastic wave theory (Meyers, 1994). This is true regardless of the source of the impulsive load; both direct impacts and rigid body skull rotations generate perturbations in the tissue. To this point, the introduction of a simple constitutive material model into the equation of momentum conservation will result in a restatement of the familiar Newton's second law as the wave equation, described by the expression,

$$\ddot{\boldsymbol{u}} = \frac{E}{\rho}\nabla^2 \boldsymbol{u}, \tag{1}$$

where $\ddot{\boldsymbol{u}}$ is the second time derivative of position, ∇^2 is the Laplacian operator, E and ρ are the elastic modulus and density of the material, respectively. From this consideration, three design parameters may have an influence on the time-dependent elastic response of the marker-tissue system: density, elastic modulus (i.e., stiffness), and spatial distribution. The differences in both density and elastic moduli of the markers and their surrounding matrix will be important design factors in minimizing the interference of embedded markers in the deformation of surrounding tissue. Additionally, the spatial distributions of markers relate to the volume and mass fraction of the marker-type material in the surrounding matrix, causing local differences in both the density and stiffness of the matrix. While density (Al-Bsharat et al., 1999; Hardy et al., 2001, 2007) and marker mass (Guettler, 2017) have been considered in prior designs of embedded markers, marker stiffness and the spacing between markers have not been broadly examined and deserve consideration.

This study was designed to provide a systematic analysis of the influence of marker density, stiffness, and pattern spacing on the deformation field in a tissue simulating material. A Taguchi L9 array (Shi et al., 2014) was used to develop nine unique marker designs using these three design variables. Each variable was tested at three values, corresponding to minimum, maximum, and mid-range quantities considered for a Post-Mortem Human Subject (PMHS) head impact study, a range developed after considering past PMHS studies (Hardy et al., 2007; Iwaskiw et al., 2018; Al-Bsharat et al., 1999; Hardy et al., 2001; Guettler, 2017; Alshareef et al., 2018, 2020). To evaluate the new markers, the impact-induced displacement response of a tissue-simulating material containing massless markers was compared to that of the same simulant material containing the embedded markers. The objective of this investigation was to identify the influence of mechanical properties of markers on the observed response of tissues, providing guidance for future marker design.

2 Experimental Methods

To gain an understanding of the sensitivity of a broader set of parameters that influence tissue motion tracking fidelity of embedded markers, we prepared a matrix of design parameters using a Taguchi L9 array (Shi et al., 2014; Rao et al., 2008). The experimental markers were prepared according to specified variations in density and elastic modulus (E). The experimental markers were arranged in a grid pattern, with a specific inter-marker spacing, cast along a single midplane of a tissue-simulant (Medical Gel #4, Humimic Medical, Greenville, SC) block (Fig. 1). The inter-marker spacing variations replicate the range of spacing patterns achievable for *ex vivo*, *in situ* insertion for a related PMHS study. The gel blocks and marker sets were

dropped from a fixed height onto an impact surface to generate displacement fields at strain rates similar to those achieved in PMHS impact testing (10^1 s^{-1}) (Hardy et al., 2007; Zhou et al., 2019).

The gel blocks were cast within a mould measuring 152 mm $\times$ 152 mm $\times$ 45 mm. These block dimensions were chosen in order to maximize the test region given the limitations of the imaging and drop-testing systems available at the time of testing. A total of 10 blocks were prepared, one for each of the nine new marker designs and one for an ink-based marker (Table 1). The ink-based markers, which were essentially massless, were used to evaluate the response of the neat material. These massless markers did not have any X-ray attenuating properties and were observed optically during experimentation with a high-speed camera.

2.1 Marker Preparation

The nine unique new markers were blends of a powdered contrast agent and a variety of elastomeric binders, which were used to achieve the desired material properties. All markers were cast using the same precision machined aluminum mould, producing a sheet of elastomeric radiopaque material, from which 2 mm diameter, 2 mm long cylindrical markers protruded. All markers were given an aspect ratio of 1; the effects of marker aspect ratio on the directionality of marker displacement was not investigated in the present work. Marker size and shape was chosen to provide clarity in imaging, and ease of manufacturing and manipulation. Barium sulfate ($BaSO_4$) was used as the contrast agent, as it is readily available in powdered form and suspends well into binder materials. At the X-ray power levels used in diagnostic imaging (25-150 keV), $BaSO_4$ has a high mass attenuation coefficient (10$< \mu/\rho <$100 cm^2/g) (Seltzer, 1995) for a material of its density (4.5 g/cm^3), and as such is commonly used in diagnostic X-ray imaging. Three different elastomeric binders were used to develop high, medium, and low stiffness markers.

The stiffest binder material was a 1:1 blend of Sylgard 184 and 527 (Dow Inc., E = 830 kPa), the intermediate stiffness binder was a 1:5 blend of Sylgard 184 and 527 (E = 130 kPa)(Palchesko et al., 2012). The least stiff binder was the same thermoplastic gel used in the tissue-simulant blocks (Gel #4, Humimic Medical) with an estimated E $\approx$ 9 kPa. This value for elastic modulus was calculated (Larson, 2017) from the manufacturer supplied durometer of 11.8 (Shore 00) using the expression,

$$E = 0.0037e^{0.0718s}, \tag{2}$$

where E is elastic modulus (MPa) and s is durometer (Shore 00). The estimated elastic modulus is consistent with similar conversions found in past tissue studies (Li et al., 2015).

Once placed in the mould, uncured marker preparations were degassed at -29 mmHg to remove small air bubbles. Markers with Sylgard-based binders were cured at room temperature, while the thermoplastic gel markers were brought to their melt temperature during casting and allowed to cool at room temperature. Variations in density were achieved by adjusting the mass ratio of elastomer binder to contrast agent. Given the random orientation of the $BaSO_4$ particles in the elastomer matrices, the elastic moduli of the resulting composites were calculated with the Reuss mixture model (Meyers and Chawla, 2009). The mixture model indicates an average increase in moduli of 30$\%$ for the composite material. Despite this increase, stiffness design parameter steps remained valid as they increased 10-fold over each other, maintaining a wide parameter space. The levels of density that were investigated were 1.05, 1.45, and 1.85 g/cm^3, compared to a density of 0.85 g/cm^3 for the neat gel block material. Given the volume of these markers of 6.3×10^{-3} cm^3, corresponding marker masses were 6.6 mg, 9.1 mg, and 11.6 mg, respectively. The levels of stiffness that were investigated were 12, 170, and 1100 kPa, compared to a stiffness of 9 kPa in the gel block material, which is comparable to the stiffness of brain tissue (Budday et al., 2015). A summary of the marker designs, their mechanical properties, and preparation variations are provided in Table 1.

To produce the thermoplastic gel test blocks, two identical reusable square moulds prepared from a 1:1 blend of Sylgard 184 and 527 were cast using a mould constructed of medium density fibreboard (MDF). These elastomeric moulds were preferred for sample preparation due to the heat resistance of the thermoset material. For each block, new tissue-simulating gel was melted completely by heating to 160°C. The liquid gel was degassed in a vacuum oven to -29 mmHg to remove entrapped air, then poured into moulds, stopping at the half-way mark in order to create the marker plane. Once the half-filled blocks were set, a printed grid pattern, corresponding to the spacing level of interest for each design, was transferred to the marker plane with ink. Markers were placed on top of the pattern. The massless markers were created by drawing approximately 2.5 mm diameter circles with an alcohol-based permanent marker at a pattern spacing of 10 mm. The negligible density of these markers permitted them to be slightly larger than the

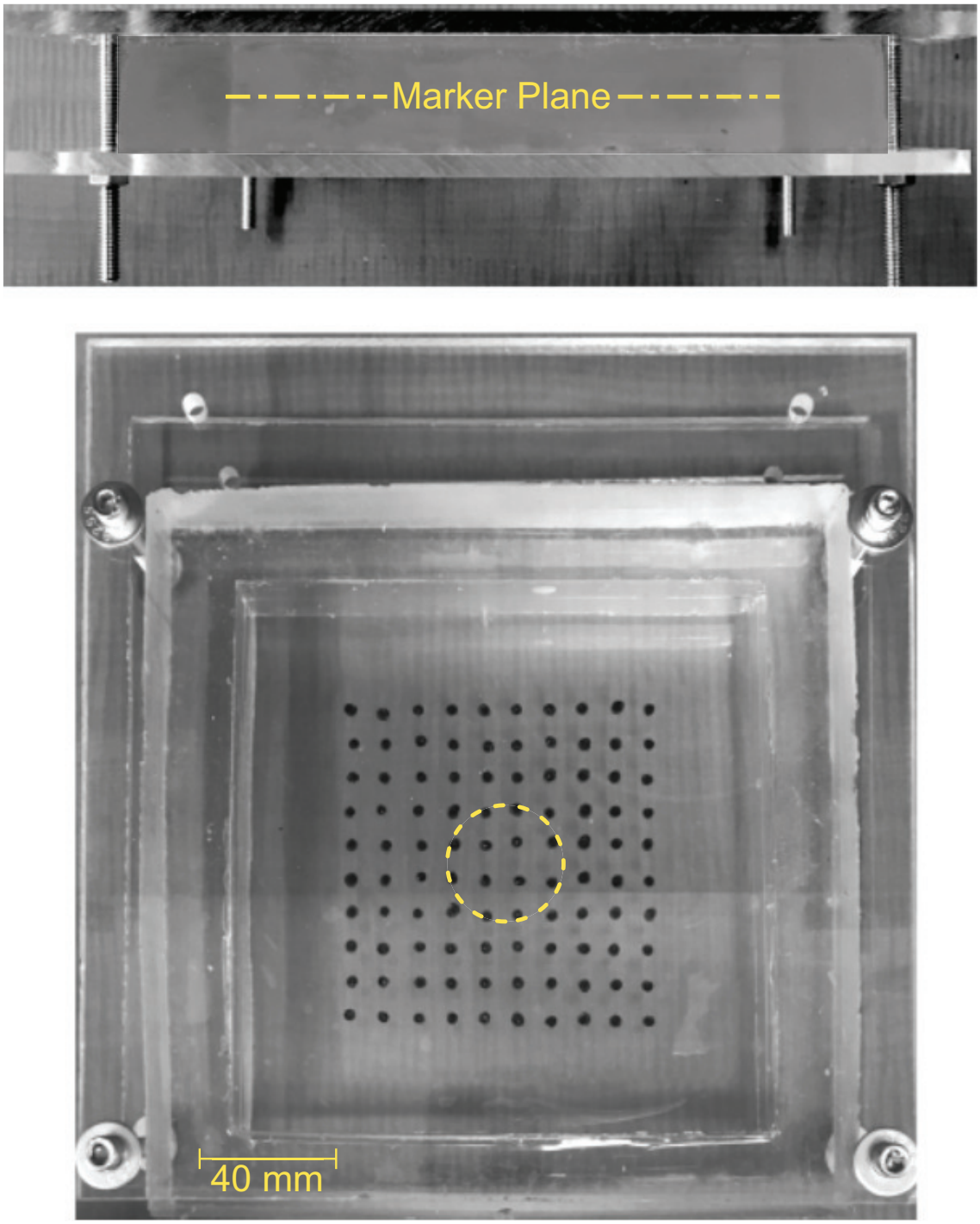

Figure 1: Top and front photographic views of the neat material block (massless markers) mounted inside the drop housing. Marker plane indicated with dashed line. Central region used for analysis is within dashed circle.

Table 1: Summary of Taguchi L9 marker designs used in the present study.

Marker Design	Density (g/cm^3)	Spacing (cm)	Stiffness (kPa)	Binder Material
1	1.05	1.0	12	Humimic # 4
2	1.05	1.5	170	Sylgard 1:5 blend
3	1.05	2.0	1100	Sylgard 1:1 blend
4	1.45	1.0	170	Sylgard 1:5 blend
5	1.45	1.5	1100	Sylgard 1:1 blend
6	1.45	2.0	12	Humimic # 4
7	1.85	1.0	1100	Sylgard 1:1 blend
8	1.85	1.5	12	Humimic # 4
9	1.85	2.0	170	Sylgard 1:5 blend
Massless	0	1.0	0	n/a

embedded markers, allowing them to be seen more clearly in optical imagery. To avoid deformation of the marker plane due to material melting or creep during the casting of the second half of the encasing thermoplastic block, this preparation was placed in a freezer at a temperature of -18°C for a minimum of 30 minutes before the remainder of the mould was filled. Completed blocks were left to set at room temperature and inspected for seams, voids, or material inhomogeneity due to the casting process. Following inspection, each specimen was wrapped in plastic and shelved to avoid indentation, creep, or compression. The Sylgard moulds were kept and later used to house each block within a drop apparatus for impact testing.

2.2 Drop Testing

To evaluate the dynamic response of the markers within the gel block, each specimen was mounted in a custom housing which was subsequently subjected to three drops onto a rigid steel anvil. A small custom drop tower was constructed for this purpose (Fig. 2). The custom housing was used to protect against boundary damage in order to facilitate multiple tests. Each block was inserted back into one of the two identical Sylgard moulds (encasements) used in the casting process. This assembly was then sandwiched between two 6.4-mm-thick acrylic plates and fastened at the corners with bolts (Fig. 1). The acrylic housing ensured that the blocks would not buckle out of plane or slide during impact. In order to provide consistent boundary conditions for each drop test, the distance between the acrylic sheets was maintained at 41 mm, resulting in a controlled, pre-strained condition.

The drop carriage on the drop tower was hoisted manually and fixed in place by an electromechanical latch at the maximum achievable system height of 76.5 cm and the specimens were dropped onto a rigid steel anvil. Following each drop, the samples and housing were inspected for damage and reset to the drop position. An electronic triggering system was used to coordinate the drop with the image capture system, allowing the recording of block motion from 50 ms before and 130 ms after impact. The purpose of the drop impact was simply to generate a reproducible dynamic loading event in the range of $10^1 s^{-1}$, which is consistent with many PMHS studies (Hardy et al., 2007; Zhou et al., 2019), but was not meant to replicate any specific impact event. Each marker assembly was dropped three times to ensure reproducibility of the results.

2.3 Data Collection

Impact image sequences were captured using the HSXR system at Carleton University at a rate of 7,500 fps. The resultant scale between camera and experiment was 3.4 $\pm$ 0.17 px/mm. The neat material block was tested using the same drop procedure, however as its markers do not attenuate X-rays, particle motion was acquired using a high-speed optical camera at the same capture rate. Refractive and reflective distortion of the optical signal through the gel was mitigated with the use of the acrylic housing; after inspection of the source video, this phenomenon had a negligible effect on the tracked motion of markers. Images were processed to improve contrast and a correction to the lens distortion was applied. A custom particle tracking code (Dutrisac, 2020) was written in MATLAB to extract the displacement of markers and housing features from collected image sequences.

To avoid conflation of internal deformation with rigid body impact motion, portions of the external housing were tracked across the time series and used to determine both the moment of impact and rebound

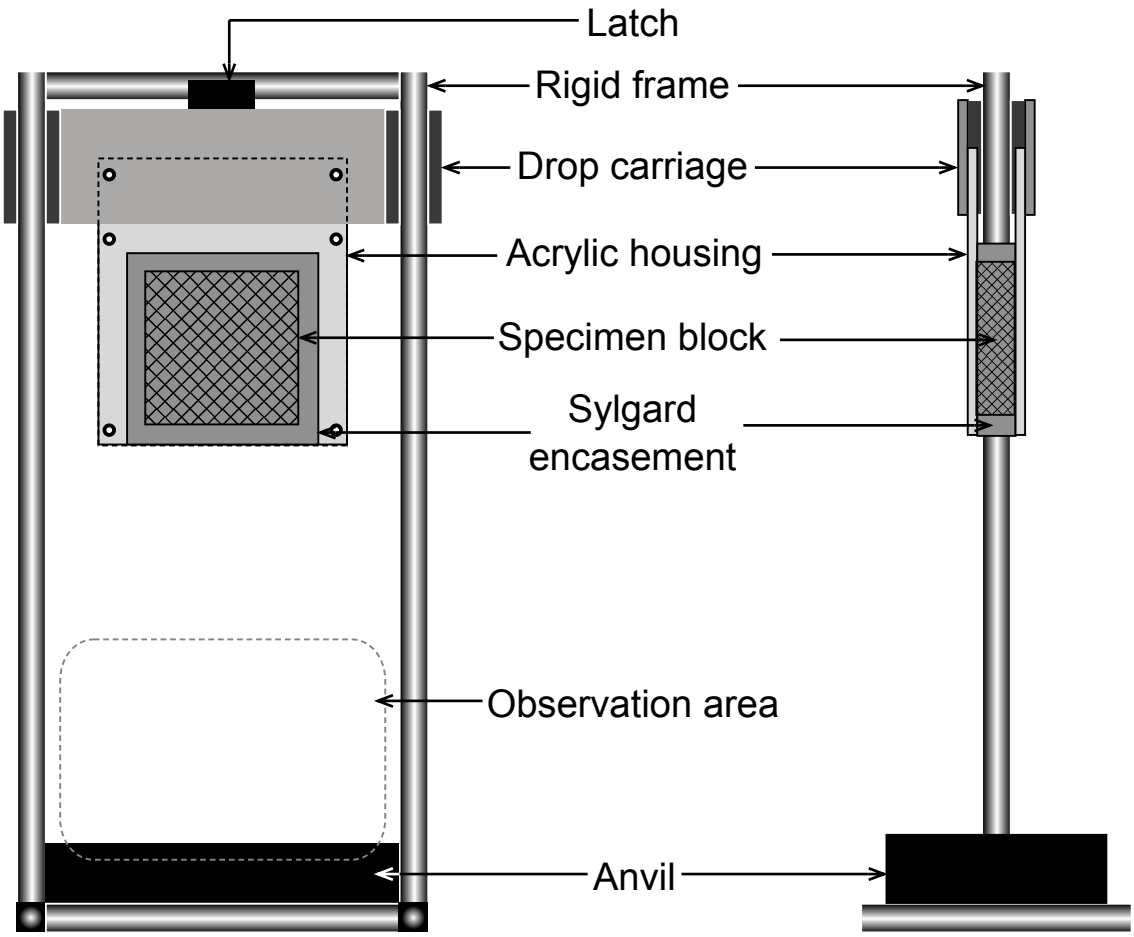

Figure 2: Front and right-section schematic views of the drop tower used in the study. Impact observation zone is denoted with a dashed line. Maximum drop height: 76.5 cm.

dynamics of each sample. For each drop, the rebound rate was linear over the 250 frame (33 ms) period of interest, at 0.11 $\pm$ 0.01 mm/frame. While the internal deformation occurred within the moving frame of reference, this rebounding rate was common across all test iterations, permitting the comparison of deformation responses.

The cohesion of the marker motion tended to dissipate into the second period of the oscillation (t>25 ms), reducing repeatability at later times. For this study, the first and second peaks of the first period response were used as the basis of comparison across all specimens, as the data was both cohesive and relevant to tissue-based impact studies(Hardy et al., 2007, 2001). The first peak represents the compressive phase following impact, and the second peak represents the relaxation and release of stored elastic energy following compression.

For the sensitivity analysis, normalized output values were necessary (Shi et al., 2014). These output values (ϕ) are defined as,

$$\phi = \frac{\chi_t - \chi_n}{\chi_n} \times 100, \tag{3}$$

where χ_n and χ_t are the measured values of the displacements for the neat material and marker-embedded material, respectively. The output value provides a measure of deviation, as caused by the presence of a marker particle. These output values (ϕ) were subsequently used in the Taguchi signal-to-noise function to make comparisons across the experimental group (Shi et al., 2014).

2.4 Analysis

The Taguchi approach to experimentation was used to reduce the number of specimen iterations required to determine parameter sensitivity(Shi et al., 2014; Rao et al., 2008). The Taguchi orthogonal array provides a method of combining variable adjustments across individual experimental trials, as shown in the marker design parameters in Table 1. This method has seen broad uptake in many fields, including the biomedical and clinical research fields to reduce the burden of experimental cost and supply limitations (Rao et al., 2008).

In order to separate the valuable data from the noise influence, the analysis uses signal-to-noise ratios (SNr) as a measure of experimental output due to varying design parameters. SNr calculations can focus on a nominal value, a lowest-is-best, or a largest-is-best output. In the case of this study, the largest-is-best evaluation was used, meaning that a large SNr corresponds to a good match between the neat material and the experimental material response. In this case, SNr is given by,

$$SNr = -10 \log_{10} \left[\frac{1}{n} \left(\sum_{i=1}^{n} \phi_i^2 \right) \right], \tag{4}$$

where ϕ is the measured output for each experiment, SNr is the signal-to-noise ratio, and n is the number of repeated trials.

The SNr for each experiment is used to evaluate the design variable influence for each of the output responses. The mean SNr for each parameter at each level is computed as

$$\overline{SNr_{PL}} = \frac{1}{k} \sum SNr_i, \tag{5}$$

where L is the parameter level, P represents the specific parameter, and k is the number of trials in which that combination appears. The index, i, corresponds to the specific trials containing the PL combination. For example, the mean SNr for the stiffness parameter at its lowest level would be the mean for experiments 1, 6, and 8, as can be seen when consulting Table 1.

To evaluate the magnitude of parameter influence, analysis of variance (ANOVA) is required (Shi et al., 2014; Oktem et al., 2007). ANOVA relates the contribution of the variance for each design parameter to the total experimental variance. The total variance (SS_t) for each experiment is equal to the sum of the design parameter variances ($\sum_{i=1}^{3} SS_i$) and the external variance, or noise (SS_e) (Oktem et al., 2007). Whereas the SNr provides information on which design parameter levels may be desirable, the magnitude provides information on the overall sensitivity of that parameter.

$$SS_t = SS_e + \sum_{i=1}^{n} SS_i \tag{6}$$

$$SS_P = \sum_{j=1}^{k} \left(\frac{(\sum SNr_L)^2}{k} \right) - \frac{G^2}{n}, \tag{7}$$

where G is the grand total from each of the n experiments and k is the number of experiments of each design parameter P at each level, L.

3 Results

The resultant first and second internal peak vertical displacements for blocks embedded with the experimental marker designs were used to identify how the individual design parameters (density, stiffness, and spacing) contributed to the deviation in the response as compared to the displacements measured in the neat material (ink markers).

3.1 Marker Displacement

Within each block, markers were indexed from left to right, top to bottom. The vertical and horizontal displacement for each marker was computed for the entire time series. An example of the horizontal and vertical motion paths for markers, shown in Fig. 3 reveals that the most repeatable 1-D displacements were seen in the central region of each block; marker motion closer to the boundary was less repeatable, likely due to minor variations in sample position between repeated tests. Within the central region (1.5 cm radius), the influence of horizontal motion resulted in an average resultant displacement of less than 1 pixel as compared to the vertical direction alone. Given this, both horizontal and transverse displacements were neglected from the analysis. Although this resulted in only a small portion of the markers being tracked, the influence of neighbouring markers remained relevant, as their existence in the matrix material inevitably altered the observed response. An investigation of marker migration revealed that between impacts, markers did not migrate relative to each other, though blocks did shift slightly within the impact assembly, creating negligible changes to starting positions (Fig. 4).

For each block, the mean vertical marker displacement for all markers in the central region, observed over three repeated drop tests, was computed, providing a single representative curve for each marker design. All specimens were tested in the same manner, each displaying a high degree of repeatability as confirmed with the computation of a 95$\%$ confidence interval (CI) for each trace. The CI was computed with a two-tailed t-test, identifying the repeatability of the response. As shown in Fig. 5, the vertical position of central markers was extracted and aligned at the moment of impact. The mean signal was computed, along with the CI. For the duration of interest, only minor variations in the motion profile occur, providing a clear picture of the impact response and its repeatability.

The first and second peak vertical displacements for each of the experimental markers are seen in Table 2, along with the associated range of the 95$\%$ CI, and the Taguchi SNr as per Equations 3 and 4. The SNr value functions as a largest-is-best representation for each response. Each response was generated from a number of input displacement traces, belonging to 3 to 12 markers depending on the grid spacing used in the design. Markers in the centre region were used as to lessen the effect of erratic motion observed at the boundary. The vertical motion profiles of these markers are shown together with the neat material profile in Fig. 6.

A comparison of the displacement response of the neat material block with marker-embedded blocks is shown in Figure 7, via the output value, ϕ (Equation 3). Here, it can be seen that Design 2 deviates least from the neat material at the first (compressive) peak, while Designs 4, 5, and 6 were the next closest to neat material response. At the second (tensile) peak, responses differ more substantially, which can be expected due to increased stochastic nature of the responses, reflected in the broader confidence intervals at later times (Table 2).

3.2 Sensitivity

While it is evident that there was some variation in the marker motion between the various marker designs, the influence of individual design parameters can be shown more clearly by examining the mean SNr for each design variable at each of its different intensity levels (L1, L2, or L3), as per Equation 5. The purpose of this process was to assess how the variations in the properties (density, stiffness, and spacing) relate

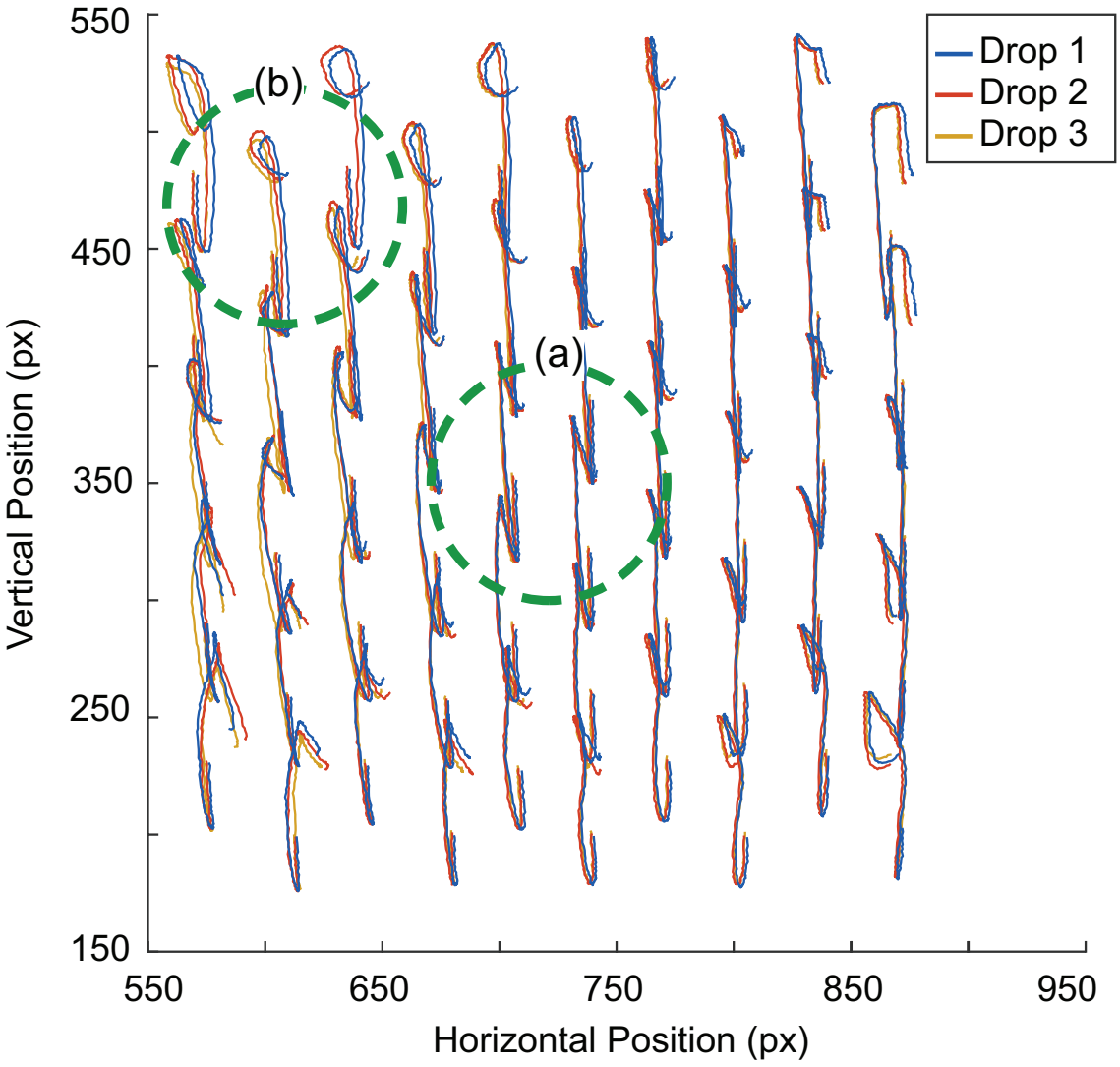

Figure 3: Example: Horizontal and vertical motion trace, Design 7, for $0 \leq t \leq 20$ms. For clarity, only odd-numbered marker paths are shown. (a) Central region, with repeatable 1-D response. (b) Boundary response is less repeatable, with increased horizontal component.

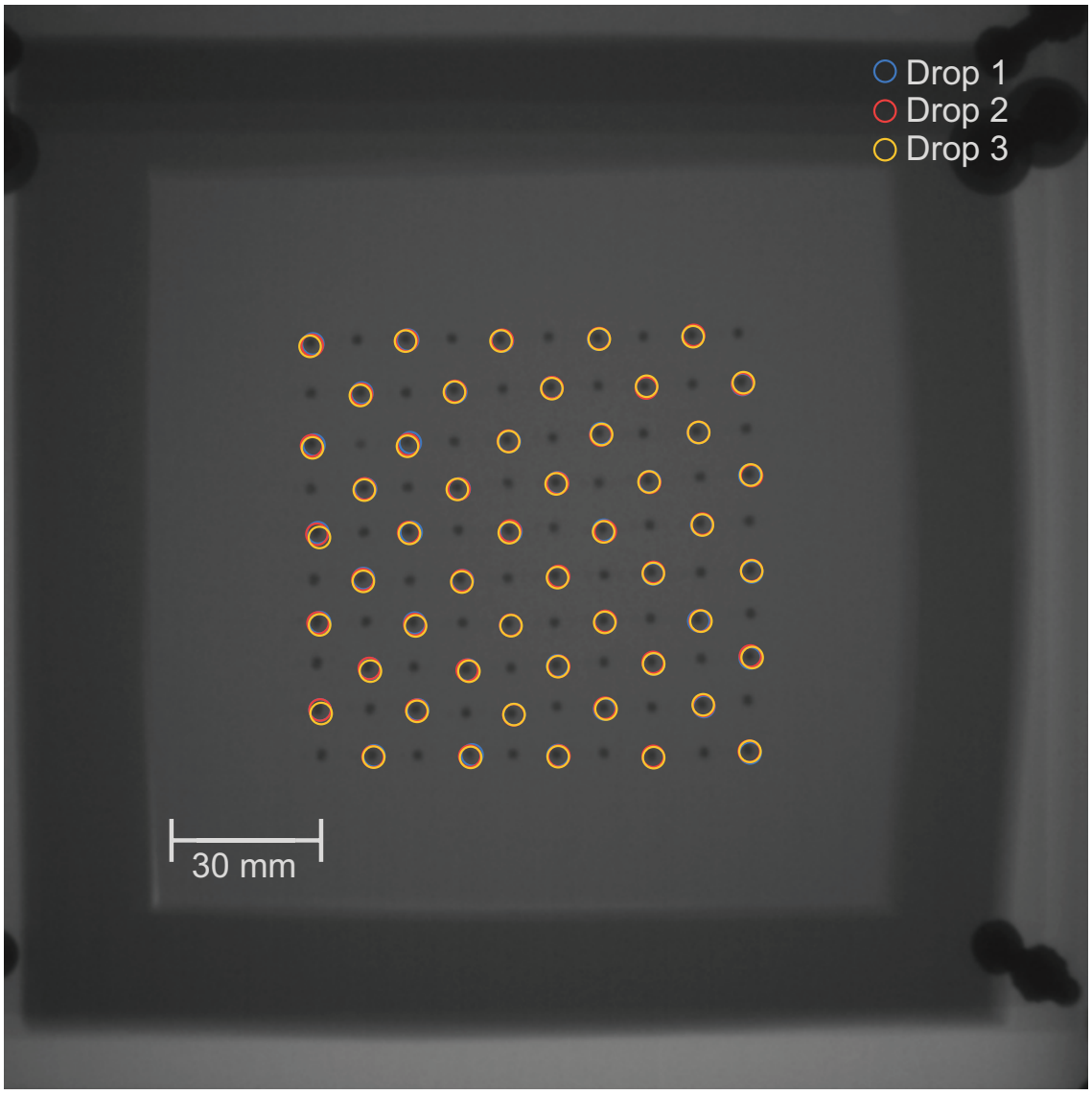

Figure 4: Overlay of drops 1 to 3 pre-impact, Design 7. For clarity, only odd-numbered markers are highlighted. Negligible shift in position signifies no migration of markers in block.

Table 2: Experimental outcomes from drop test and respective SNr.

Experiment	First Peak			Second Peak		
	(mm)	C.I. $(\pm mm)$	SNr(dB)	(mm)	C.I. $(\pm mm)$	SNr (dB)
Neat	11.8	0.2	–	18.6	0.9	–
1	10.6	0.3	19.6	20.3	0.4	21.1
2	11.5	0.4	31.1	16.9	0.9	20.6
3	8.1	0.4	10.0	22.8	0.8	13.0
4	12.2	0.3	30.1	18.7	0.6	45.5
5	12.2	0.3	29.0	10.5	0.5	7.2
6	11.2	0.1	25.4	20.7	1.0	19.3
7	10.2	0.2	17.3	17.0	0.2	20.9
8	9.6	0.2	14.8	17.9	0.3	27.7
9	10.3	0.2	18.0	20.4	0.4	20.7

to deviations in the material response. For each design variable, the spread of the means of SNr values highlights how sensitive the output metric is to changes in the variable intensity (Table 1). These results

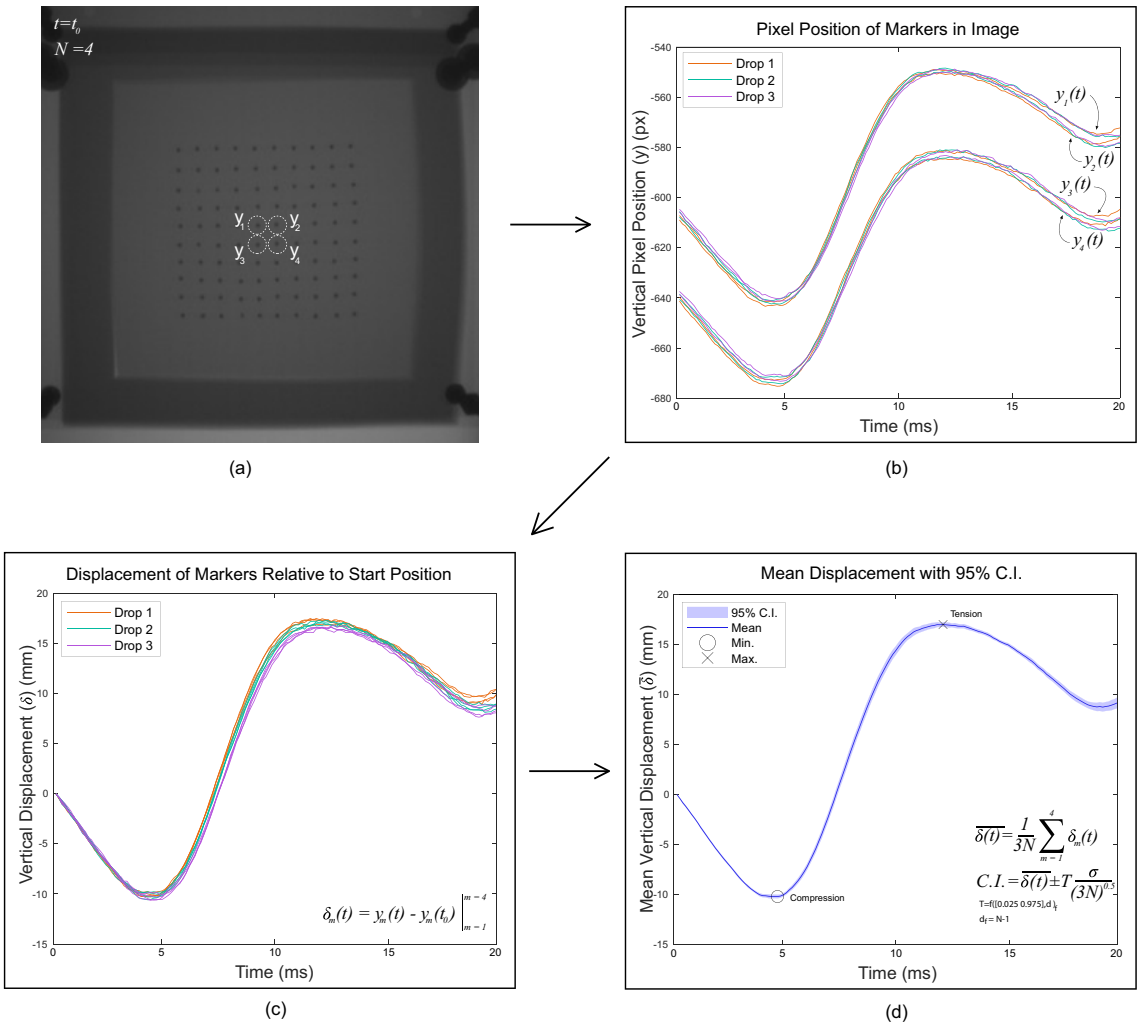

Figure 5: Example: Design 7 vertical displacement, extracted by selection of central markers (a) for pixel position tracking. Pixel positions (b), were converted from pixels to millimetres and normalized to their moment-of-impact positions, creating a displacement curve (c). Displacements were used to generate mean displacement and CI curve (d), where the peak first and second displacements were evaluated. Moment of impact occurs at t = 0 ms, with the first and second peaks occurring at approximately 4 ms and 13 ms, respectively.

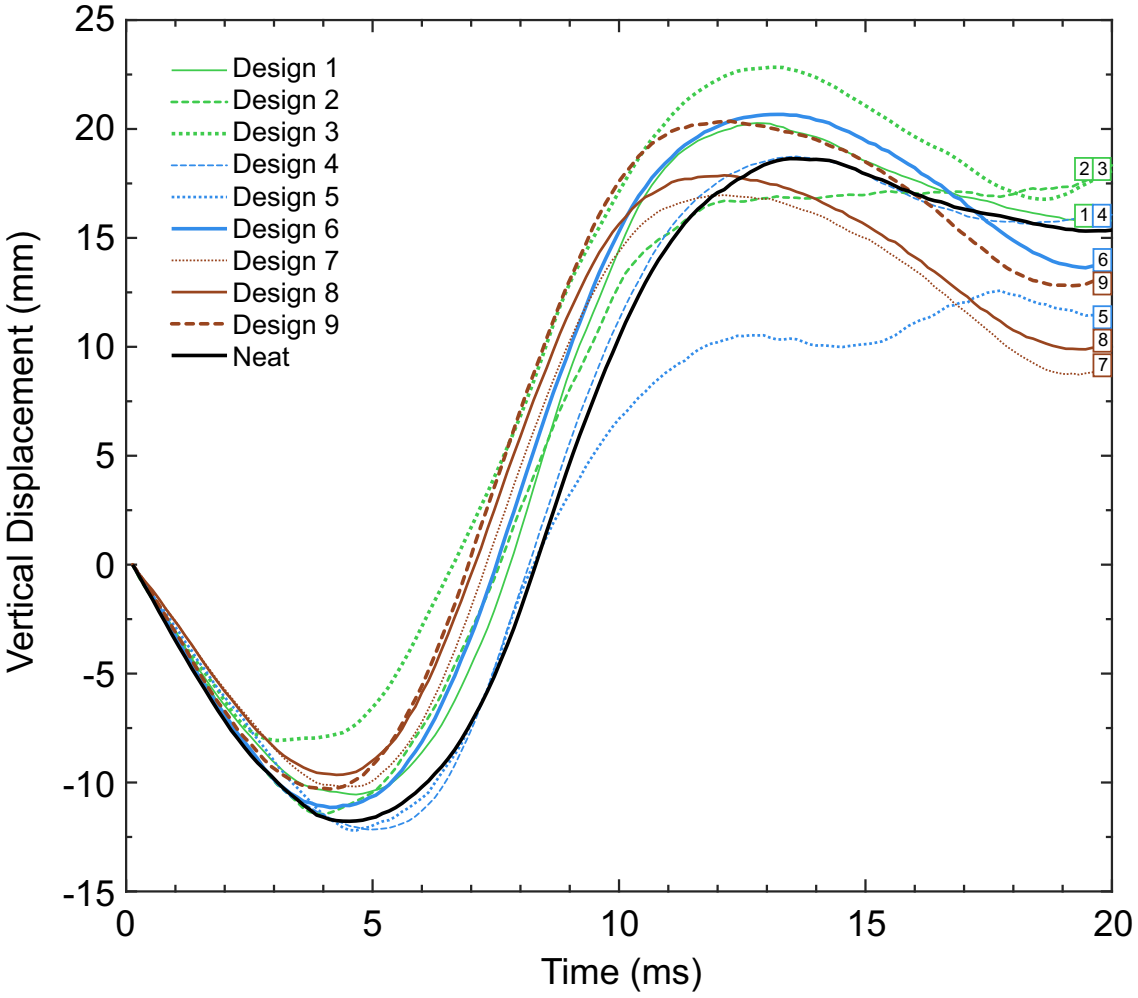

Figure 6: Mean vertical response of central markers within each test block. Curves are aligned at the moment of impact.

Table 3: Mean SNr at Peak 1

	Mean SNr			
Parameter	L1	L2	L3	Spread
Density	20.2	28.2	16.7	11.4
Spacing	22.3	24.9	17.8	7.1
Stiffness	20.0	26.4	18.8	7.6

are shown in Tables 3 and 4 for displacement peak 1 and peak 2, respectively. The results demonstrate that the parameters with the highest influence in the displacement at the first and second peak were different. In Table 3, representing the response of the markers in the first displacement peak, the greatest range of motion was associated with changes in marker density. In Table 4, responses in the second displacement peak were associated with the greatest spread in stiffness and were not strongly correlated to marker density.

The comparison of mean SNr provides insight into how each design variable contributes to the deviation of the output, however it does not evaluate the strength of the contribution. Using the ANOVA described in Equations 6 and 7, the sensitivity of both the input design variables and the external noise were evaluated. These results are shown in Table 5 as representative percentages of the total sensitivity. The sensitivity values reinforce what was learned from the SNr comparisons, suggesting that early on in the deformation process, marker density (46$\%$) played a significant role in ensuring the fidelity of the deformation field being measured. Marker stiffness (22$\%$) and spacing (18$\%$) were less significant than density, but still influence the deformation process and must be considered. As the deformation progresses, the matrix deformation became extremely sensitive to marker stiffness and spacing sensitivity (39$\%$, 28$\%$, respectively), while density was substantially less influential (6$\%$). External noise also contributed, which is related to uncontrollable factors (Rao et al., 2008), which increased from the first to second peak (14$\%$, 27$\%$).

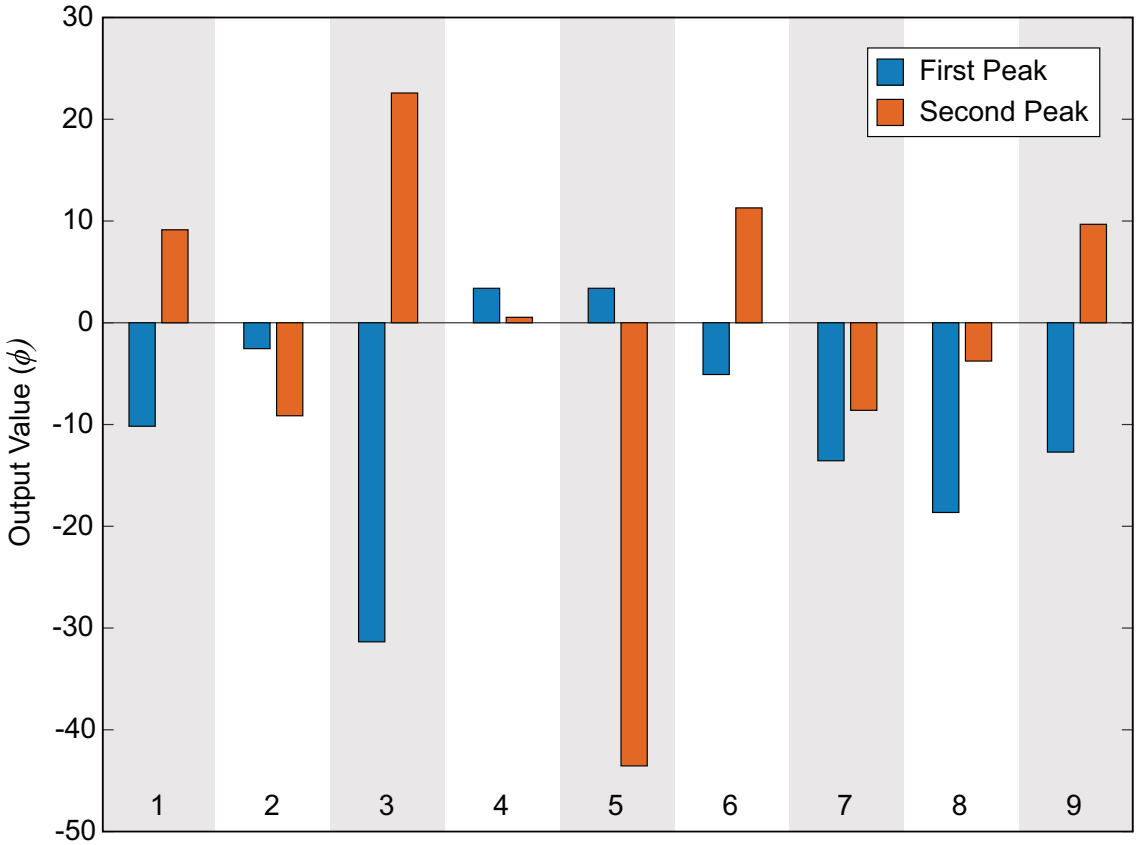

Figure 7: Output value, ϕ, as computed with Equation 3, for each design at first and second peak values.

Table 4: Mean SNr at Peak 2

	Mean SNr			
Parameter	L1	L2	L3	Spread
Density	18.2	24.0	23.1	5.7
Spacing	29.2	18.5	17.6	11.5
Stiffness	22.7	28.9	13.7	15.2

Table 5: Parameter sensitivity ($\%$) from ANOVA

Parameter	Peak 1	Peak 2
Density	46	6
Spacing	18	28
Stiffness	22	39
External Noise	14	27

4 Discussion

The results of this study can be examined in two distinct ways. First, a marker "performance" can be established by evaluating which markers yielded the least deviation from the neat material response at their first and second displacement peaks. Second, using the results from the sensitivity study and ANOVA, a range of optimal design parameters can be described, helping to minimize the interference of markers in the deformation of the matrix material for future work.

Fig. 8 provides a closer look at the variability of different marker groupings in the medium and high stiffness range (Fig. 8a and 8b) as well as in the medium and high density range (Fig. 8c and 8d). With these groupings, although there were confounding factors, it is clear that a medium stiffness material was preferable to a high stiffness marker material. In this context, medium stiffness and hard stiffness markers had elastic moduli that were 2 and 3 orders of magnitude higher than the matrix, respectively. Similarly, high density marker materials resulted in a consistently lower displacement response of the matrix, and large variability on the second peak. The medium density markers did not greatly influence the first peak displacement of the matrix gel, but the influence in second peak response was dominated by marker stiffness, as seen from high-stiffness Design 5 (E =1100 kPa). In the context of the present work, medium and high density markers were defined as markers with density ratios of 1.7 and 2.2, respectively.

The trends were less clear when examining the effects of marker spacing. For Design 4 (E =170 kPa, ρ =1.45 g/cm^3), a marker spacing of 10 mm, or 5 marker diameters, appears to be suitable, given its performance, yet Design 1 (E =12 kPa, ρ =1.05 g/cm^3), with the same spacing, yielded a poor match to the neat material response. It may be possible that the specific blend of parameters in Design 4 outweighed the influence of the minimal spacing distance, which is observable in the response of Design 1. Examining the response of the block containing Design 6 (E =12 kPa, ρ =1.45 g/cm^3), whose spacing was at a the maximum, 10 marker diameters (20 mm), the response was not a perfect match to the neat material, but it is among the less deviating responses.

Considering both the first and second peaks, along with the sensitivity analysis (Table 5), it is clear that both density (46$\%$) and stiffness (39$\%$) must be equally considered when designing embedded markers. However, precisely matching the matrix density and stiffness is not critical to reducing the influence of the markers on the deformation field; a marker density below 175$\%$ of that of the matrix and a marker stiffness below 1.0 MPa appears to be beneficial. Design 4 falls within this optimal range and was the best performing marker in this study. In contrast, high density designs (7, 8, 9) and high stiffness designs (3, 5, 7) were among the worst performers when first and second peak displacements were considered together (Fig. 8b and 8d, respectively). Though consideration of pattern spacing is valuable, this design parameter results in a lower overall influence on the matrix (28$\%$ at the second peak). This balance of properties is reflective of the variables known to affect the dynamics of matrix deformation and strain equilibration based on Equation 1. Adjustments to total marker mass via size and density will influence inertia, while density and stiffness, coupled with spacing of markers, will affect the material sound speed(Meyers, 1994). As such, no specific formula for marker design is presented, rather a recommendation to help narrow down the design space.

Both image-based and ultrasound-based particle tracking systems have been used in PMHS impact studies

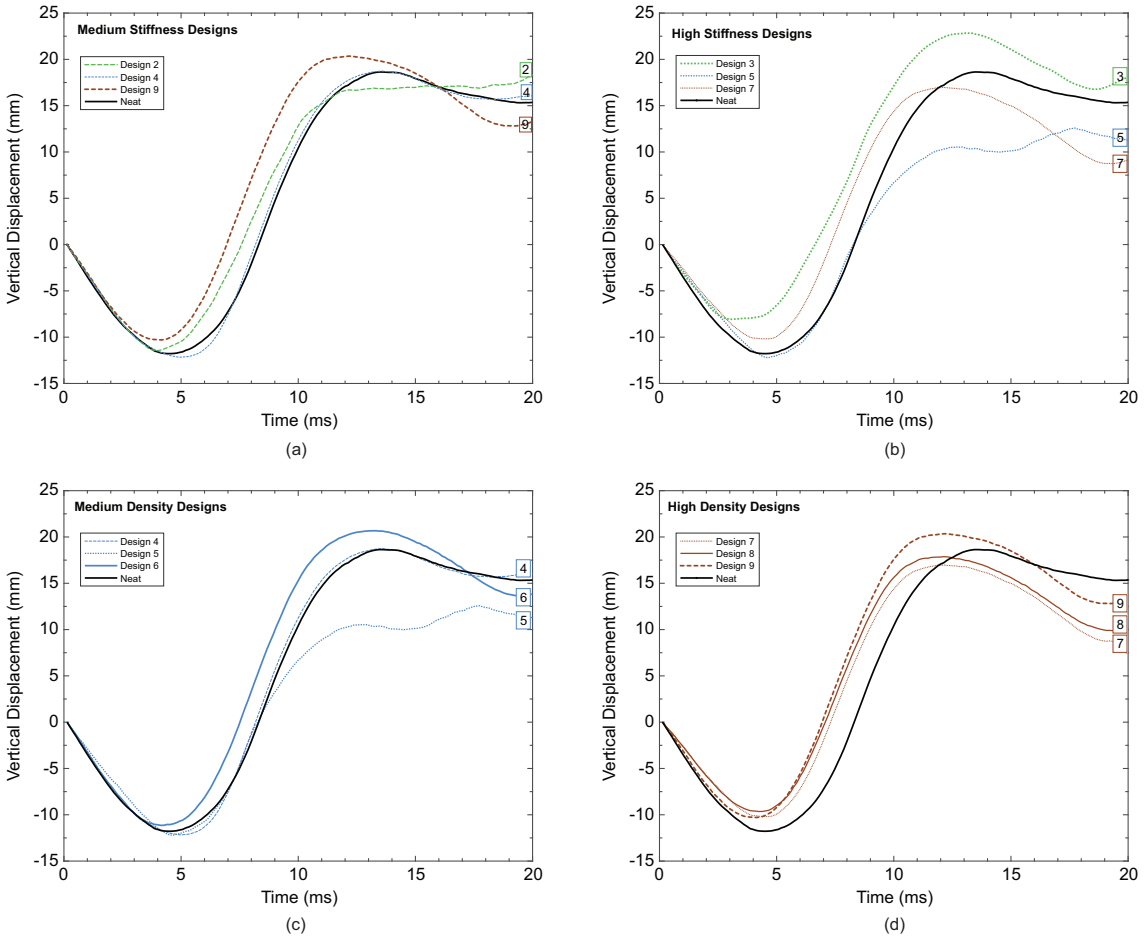

Figure 8: The displacement response of the massless marker (neat material) to various marker groupings with (a) medium stiffness (170 kPa), (b) high stiffness (1100 kPa), (c) medium density (1.45 g/cm^3), and (d) high density (1.85 g/cm^3). Note the density and stiffness of the matrix material were 0.85 g/cm^3 and 9 kPa, respectively.

with a high degree of precision. Although these systems are well suited to identify how tracking particles move following an impact, the particles themselves introduce their own uncertainty. These results confirm that the insertion of any marker that is used to track deformation will change the deformation of the surrounding matrix material. The measurements comparing marker displacements to neat material demonstrate that the fidelity of the local deformation patterns were affected by the presence of the markers, leading to errors that were related to the comparative material properties of the markers and matrix material. This has significant implications to the use of marker tracking data within brain tissues of cadaveric specimens and our understanding of their accuracy, which should not be confounded with marker tracking precision. Locating a marker with high precision is of the utmost importance; however, if the marker is in the wrong location due to its influence on tissue deformation, the measurement is precise but not an accurate representation of the natural physical response of the tissue. The results of the present work demonstrate the importance of proper marker design to improve measurement accuracy. Although it was not verified in the present work, we expect that large marker aspect ratios and anisotropic confinement of the markers through tethers may result in directional variability of marker disruption of the deformation field and associated errors.

5 Conclusion

The inclusion of any tracking marker into a deformable matrix will alter the response of that matrix to impulsive loading, making it a challenge to measure the deformation. The parametric design and subsequent sensitivity analysis embedded tracking markers has revealed that density, stiffness, and marker spacing each play a role in altering the natural response the matrix. The least influential marker had a density

and stiffness in the middle of the design space (ρ =1.45 g/cm^3, E=170 kPa), with a minimal spacing distance (10 mm). Other low-influence markers included those with with low stiffness and density, but had broader spacing distances of 15-20 mm. This group deviated least during the first, compressive, phase of displacement. Within this group, all properties except high density and high stiffness were represented, clearly indicating that carefully selected combinations of parameters, and not individual qualities, result in a reduction deviation from the neat material response. It appears that low to medium density, up to 175$\%$ of the matrix material density, and low to medium stiffness, below 1.0 MPa, make the best markers and minimize the influence on matrix deformation. Markers outside of this range tend to cause greater deviations from the neat material response. Although less significant, marker spacing between 7 and 10 marker diameters may help to reduce volume fraction matrix stiffening effects, improving the similarity to the neat material response.

The uncertainty on displacement measurements and subsequently calculated strain values is a function of marker design, placement, and time-after-impact. This work provides a clearer understanding of the errors associated with the measured displacement of tissues through the use of embedded markers, as well as providing a basis for the future design of such markers. The results of this work illustrate the importance of properly quantifying the errors associated with strain fields and FE model validation calculated on the basis of markers previously used in prior PMHS studies.

While this study is specific to the dynamic loading and coupling of tracking particles in soft tissue, these findings highlight the importance of evaluating gauge interference for other loading types and measurement configurations. Under quasi-static loading or low-rate cyclic loading, dynamic coupling may not be a concern. However, the inclusion of particles may, for example, stiffen or weaken a matrix, altering the natural mechanical properties, leading to a loss of accuracy in the measurement. Care should be taken under these circumstances to develop measurement systems that minimally, or predictively, influence those natural responses.

6 Acknowledgements

Funding for this work was provided by the Canadian Institutes of Health Research and the Natural Sciences and Engineering Research Council of Canada through the Collaborative Health Research Program (CPG-151967). The cineradiography equipment was funded through the Canada Foundation for Innovation and Ontario Research Fund (project 32933). SD received funding through the Ontario Graduate Scholarship program.

References

Al-Bsharat, A. S., Hardy, W. N., Yang, K. H., Khalil, T. B., Tashman, S., and King, A. I. (1999). Brain/skull relative displacement magnitude due to blunt head impact: New experimental data and model. *Stapp Car Crash Conference Proceedings*, P-350(724):321–332.

Alshareef, A., Giudice, J., Forman, J., Salzar, R., and Panzer, M. (2018). A novel method for quantifying human in situ whole brain deformation under rotational loading using sonomicrometry. *Journal of Neurotrauma*, 35(5):780–789.

Alshareef, A., Giudice, J., Forman, J., Shedd, D., Reynier, K., Wu, T., Sochor, S., Sochor, M., Salzar, R., and Panzer, M. (2020). Biomechanics of the human brain during dynamic rotation of the head. *Journal of Neurotrauma*, 37(13):1546–1555.

Budday, S., Nay, R., de Rooij, R., Steinmann, P., Wyrobek, T., Ovaert, T. C., and Kuhl, E. (2015). Mechanical properties of gray and white matter brain tissue by indentation. *Journal of the mechanical behavior of biomedical materials*, 46:318–330.

Chu, T. C., Ranson, W. F., and Sutton, M. A. (1985). Applications of digital-image-correlation techniques to experimental mechanics. *Experimental Mechanics*, 25(3):232–244.

Dutrisac, S. (2020). *A Study of the Impact Response of Discrete Regions of the Human Cadaver Brain*. Carleton University, Ottawa, Ontario, Canada.

Guettler, A. (2017). *Quantifying the Response of Relative Brain/Skull Motion to Rotational Input in the PMHS Head*. Virginia Polytechnic Institute and State University, Blacksburg, Virginia, USA.

Hardy, W., Foster, C., Mason, M., Yang, K., King, A., and Tashman, S. (2001). Investigation of head injury mechanisms using neutral density technology and high-speed biplanar x-ray. *Stapp Car Crash Journal*, 45:337–368.

Hardy, W., Mason, M., Foster, C., Shah, C., Kopacz, J., Yang, K., King, A., Bishop, J., Bey, M., Anderst, W., and Tashman, S. (2007). A study of the response of the human cadaver head to impact. *Stapp Car Crash Journal*, 51:17–80.

Hu, Z., Xu, T., Wang, X., Xie, Z., Luo, H., He, Y., Guo, L., Li, Y., Gan, R., and Lu, H. (2018). Fluorescent digital image correlation techniques in experimental mechanics. *Science China Technological Sciences*, 61(1):21–36.

Iwaskiw, A. S., Ott, K. A., Armiger, R. S., Wickwire, A. C., Alphonse, V. D., Voo, L. M., Carneal, C. M., and Merkle, A. C. (2018). The measurement of intracranial pressure and brain displacement due to short-duration dynamic overpressure loading. *Shock Waves*, 28(1):63–83.

Karrholm, J., Gill, R., and Valstar, E. (2006). The history and future of radiostereometric analysis. *Clinical Orthopaedics and Related Research*, 448:10–21.

Larson, K. (2017). Can you estimate modulus from durometer hardness for silicones? yes, but only roughly ... and you must choose your modulus carefully! White paper, Dow Chemical Company.

Lauret, C., Hrapko, M., van Dommelen, J. A. W., Peters, G. W. M., and Wismans, J. S. H. M. (2009). Optical characterization of acceleration-induced strain fields in inhomogeneous brain slices. *Medical Engineering & Physics*, 31(3):392–399.

Li, N., Sutton, M. A., Schreier, H. W., Turner, J. L., and Mani, N. (2016). Strain measurements through optimized particle tracking in volumetric images: Methodology and error assessment. *Experimental Mechanics*, 56(7):1281–1291.

Li, W., Belmont, B., and Shih, A. (2015). Design and Manufacture of Polyvinyl Chloride (PVC) Tissue Mimicking Material for Needle Insertion. *Procedia Manufacturing*, 1:866–878, ISSN: 23519789, DOI: 10.1016/j.promfg.2015.09.078, http://dx.doi.org/10.1016/j.promfg.2015.09.078.

Meijering, E., Dzyubachyk, O., and Smal, I. (2012). Methods for cell and particle tracking. *Methods in Enzymology*, 504:183–200.

Meyers, M. A. (1994). *Dynamic Behavior of Materials*. John Wiley & Sons Ltd., ISBN: 9780470172278, DOI: https://doi.org/10.1002/9780470172278.ch2, https://onlinelibrary.wiley.com/doi/abs/10.1002/9780470172278.ch2.

Meyers, M. A. and Chawla, K. K. (2009). *Mechanical behavior of materials*. Cambridge University Press, Cambridge ; New York, 2nd ed edition, ISBN: 9780521866750.

Oktem, H., Erzurumlu, T., and Uzman, I. (2007). Application of Taguchi optimization technique in determining plastic injection molding process parameters for a thin-shell part. *Materials and Design*, 28(4):1271–1278, ISSN: 18734197, DOI: 10.1016/j.matdes.2005.12.013.

Palanca, M., Tozzi, G., and Cristofolini, L. (2016). The use of digital image correlation in the biomechanical area: a review. *International biomechanics*, 3(1):1–21.

Palchesko, R. N., Zhang, L., Sun, Y., and Feinberg, A. W. (2012). Development of polydimethylsiloxane substrates with tunable elastic modulus to study cell mechanobiology in muscle and nerve. *PLoS One*, 7(12):e51499.

Rao, R. S., Kumar, C. G., Prakasham, R. S., and Hobbs, P. J. (2008). The Taguchi methodology as a statistical tool for biotechnological applications: A critical appraisal. *Biotechnology Journal*, 3(4):510–523, ISSN: 18606768, DOI: 10.1002/biot.200700201.

Schreier, H., Orteu, J. J., and Sutton, M. A. (2009). *Image Correlation for Shape, Motion and Deformation Measurements*. Springer US.

Seltzer, S. (1995). *Tables of X-Ray Mass Attenuation Coefficients and Mass Energy-Absorption Coefficients, NIST Standard Reference Database 126*. National Institute of Standards and Technology, DOI: 10.18434/T4D01F, http://www.nist.gov/pml/data/xraycoef/index.cfm.

Shi, K., Zhang, D., Ren, J., Yao, C., and Yuan, Y. (2014). Multiobjective optimization of surface integrity in milling tb6 alloy based on taguchi-grey relational analysis. *Advances in Mechanical Engineering*, 6:280313.

Synnergren, P., Goldrein, H., and Proud, W. (1999). Application of digital speckle photography to flash x-ray studies of internal deformation fields in impact experiments. *Applied Optics*, 38:4030—-4036.

Whyte, T., Liu, J., Chung, V., McErlane, S. A., Abebe, Z. A., McInnes, K. A., Wellington, C. L., and Cripton, P. A. (2019). Technique and preliminary findings for in vivo quantification of brain motion during injurious head impacts. *Journal of Biomechanics*, 95:109279.

Zhao, W. and Ji, S. (2020). Displacement- and strain-based discrimination of head injury models across a wide range of blunt conditions. *Annals of Biomedical Engineering*, 8(9):1661–1677.

Zhou, Z., Li, X., Kleiven, S., Shah, C., and Hardy, W. (2019). A reanalysis of experimental brain strain data: Implication for finite element head model validation. *In SAE 62nd Stapp Car Crash Conference*.